Role of convection in thin-layer electrodeposition

John M. Huth,* Harry L. Swinney,† and William D. McCormick
Center for Nonlinear Dynamics and the Department of Physics, The University of Texas, Austin, Texas 78712

Alexander Kuhn and Françoise Argoul‡
Centre de Recherche Paul Pascal, Avenue Schweitzer, 33600 Pessac, France
(Received 11 October 1994)

Measurements of fluid motion during thin-layer electrochemical growth reveal that convection arising from concentration gradients that are transverse to gravity is immediate and substantial for experimental conditions typical to many studies in the literature. A particle tracking technique is used to determine and follow the time evolution of the convective velocity field. The contribution of buoyancy driven convection to local and global transport is compared to that arising from diffusion. A transition is observed from a regime in which the convection rolls near each electrode grow as $t^{4/5}$ to a regime with the roll size growing as $t^{1/2}$. Convection generated by electric fields can also be important in electrodeposition experiments; the measured electroconvective velocities are found to be much smaller than those predicted by the theory of Fleury and Chazalviel.

PACS number(s): 81.15.Pq, 47.20.Bp, 47.65.+a, 82.45.+z

I. INTRODUCTION

Thin-layer electrodeposition has achieved widespread popularity in recent years as a paradigm for the experimental study of pattern formation during growth [1,2]. The patterns formed under some conditions are fractals and have been analyzed assuming that diffusion is the dominant mode of chemical transport. However, convection is inevitable in electrodeposition and in most cases convective effects are not negligible, as we shall show.

Electrodeposition experiments could be accurately described by a purely diffusive model if buoyancy driven convection and electric field effects were negligible and if the chemical kinetics were sufficiently fast. One simple purely diffusive picture, the diffusion limited aggregation model proposed by Witten and Sander [3], has been found to provide a reasonable description of the fractal structure of growing electrodeposition clusters under conditions of low ionic concentration and low applied voltage [4–6]. This model with independent random walkers continues to guide research, yielding surprising statistical regularities in randomly constructed patterns [7–10].

A purely diffusive model, however, cannot describe the observed cooperative effects such as oscillatory growth [11,12], certain patterned states (e.g., dense or comblike structures [13,14]), and transitions in the global morphology of a growing cluster [15,16]. Under many conditions, *ionic migration* is a more important transport mode than diffusion, and the drift of chemical impurities can alter patterns dramatically [17–21]. Complicated dynamical behavior is observed when multiple chemical reaction pathways are available [12,22].

The existence of convective transport in electrodeposi-

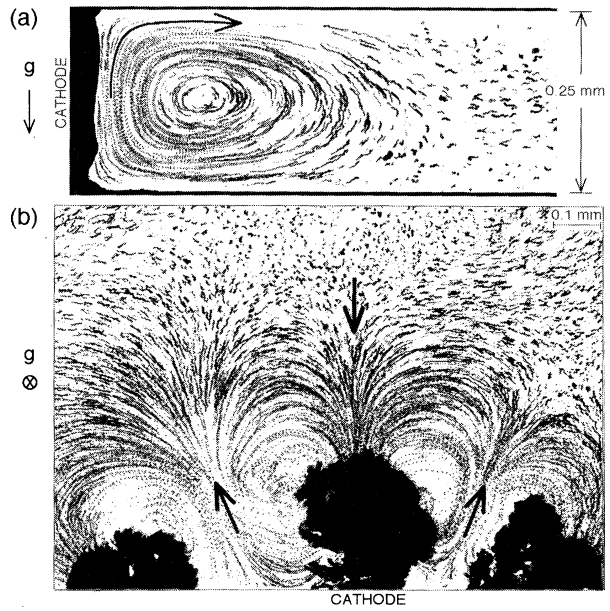

FIG. 1. Convective motion in electrodeposition visualized with tracer particles in (a) a side view, showing particle trajectories in a vertical plane, and (b) a top view, showing particle trajectories in a horizontal plane. The convective motion is driven primarily by buoyancy in (a) and by the electric field in (b). In each case, 36 digital snapshots, spanning an interval of 6 s, are superposed to show the motion of tracer particles. The arrows indicate the direction of flow. The conditions are as follows: (a) $t \approx 15$ s, the cell is $17 \times 1 \times 0.25$ mm^3, [$ZnSO_4$]=0.2M, and $J = 40$ mA/cm^2; (b) $t \approx 840$ s, the cell is $25 \times 25 \times 0.1$ mm^3, [$CuSO_4$]=0.01M, and $J = 4$ mA/cm^2.

*Electronic address: huth@chaos.ph.utexas.edu
†Electronic address: swinney@chaos.ph.utexas.edu
‡Electronic address: argoul@crpp.u-bordeaux.fr

 ©1995 The American Physical Society

tion has long been recognized and is a major reason for the use of thin gap cells [4]. However, the importance of convection has become appreciated only with the recent observations of concentration variations [23,24].

We have developed a particle tracking technique that has enabled us to make the first direct measurements of convective motions in electrodeposition. Measurements are made not simply of the velocity at a point, but of the entire velocity field in a plane, either parallel or perpendicular to the electrodes. The time evolution of the velocity field during the growth process is determined using a digital imaging system to follow large numbers (typically 200) of small, neutrally buoyant tracer particles.

Buoyancy driven convective motion is inevitable whenever deposition establishes a concentration gradient with a component perpendicular to the direction of gravity. Figure 1(a) is an example of data for buoyancy driven convection: tracer particle trajectories are shown in a vertical plane perpendicular to the electrodes. Our observations indicate that, even in thin gap cells, such fluid motion develops quickly ($\sim$ 15 s) after a voltage is imposed across the electrodes.

For some conditions, fluid motion arises primarily from electric field rather than buoyancy effects, as Fig. 1(b) illustrates: the particle trajectories are shown in a horizontal plane, parallel to the electrodes. The importance of this *electroconvection* has been recently emphasized particularly in the work of Fleury and co-workers [25–28], who have proposed a model that captures the main features of the flow; however, although measurements of concentration variations have tested some aspects of the model, the predictions have not previously been tested with direct velocity field measurements.

Our data for the velocity field as a function of cell depth, current density, and electrolyte concentration help in distinguishing different mechanisms driving the convection motions and help elucidate the role of convective processes in electrodeposition. After describing our experimental approach in Sec. II, we present in Sec. III the results for buoyancy driven convective transport for a range of conditions typical of past electrodeposition studies. In Sec. IV we examine electroconvection, comparing the predictions of the Fleury model with our velocity measurements, and we present evidence suggesting an additional electric-field-driven convection mode observed in electrodeposition: *electro-osmosis*. Section V is a discussion.

II. EXPERIMENTAL SYSTEM

Experiments are done in a thin layer of metal salt solution (ACS reagent purity $ZnSO_4$ or $CuSO_4$ from Aldrich, 0.01–0.5M) confined between parallel glass plates separated by a small gap distance d and terminated at either end by zinc or copper wire electrodes of length w, separated by a distance l (Fig. 2). The cell width w and length l are usually large compared to the gap d. Electric current is driven through the cell, causing positive metal ions to be extracted from solution and electrodeposited onto the cathode, building a complex, branching metallic

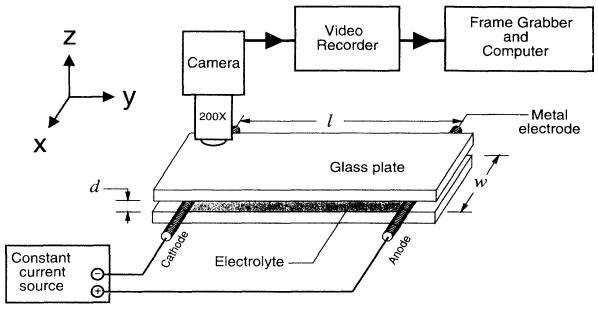

FIG. 2. Schematic diagram of the experimental system. A fixed current imposed upon the cell drives deposition at the cathode and dissolution at the anode.

structure. The anode injects metal ions into the solution at the far end of the channel, conserving the current and keeping the total number of ions in the cell fixed. The current is maintained constant to within 0.02% or better.

Fluid flow is visualized with nonionic, neutral density tracer particles ($1-3$ μm diameter; 10^8 cm^{-3}) added to the electrolyte solution. Figure 1(b) is a *top* view of the experiment, useful for visualizing electroconvective fluid motion occurring within the quasiplane of the growth. Buoyancy driven flow, however, occurs perpendicular to the quasiplane of growth and is more effectively studied by viewing from the *side*, as in Fig. 1(a). Cells with small w are used when viewing from the side, but in all side-view experiments $w \geq d$. The microscope objectives used have a very short depth of field, so that only those particles lying within about 15 μm of the focal plane are observable.

A stepper motor and translation stage position the cell. An Olympus Ultra Long Working Distance microscope objective collects collimated white light transmitted through the cell and images it on the charge coupled device camera. Images are recorded on a Sony Extended Definition Beta videotape system. An Apple Macintosh IIfx personal computer with a Data Translation Quick Capture electronic frame grabber card digitizes video data with 256 gray levels at up to 15 frames/s and 0.9 μm /pixel resolution when the 200× microscope lens system is used. The National Institute of Health's public domain software package IMAGE is used to superimpose digital snapshots to produce composite streak images [29].

Particles are tracked using software developed by Pervez and Solomon [30]. A sequence of video images containing tracer particles is digitized and background lighting inhomogeneities are subtracted. The first stage of analysis generates the (x, y) coordinates of all the particles present in a given frame. A "particle" is identified as a contiguous region of pixels having gray scale intensity values above a specified level and falling within a specified size range. A center-of-mass calculation is performed on the distribution of pixel intensity values within each such identified region, generating a list of floating-point coordinate pairs for all particles found at a given time. The second stage of analysis reads this list and assigns every (x, y) pair to the trajectory (t, x, y) associated with an

individual particle, using the particle's history to predict its upcoming location. Typically, a few hundred particles are detected in each frame and individual particles are often followed for the duration of the tracking experiment unless advected out of the field of view.

To measure the evolution of the concentration field, a 10× microscope objective incorporating a two-arm Michelson interferometer (Ealing model 25-0092) is used with helium-neon laser light. Standard microscope slides ($76 \times 25 \times 1$ mm^3) confine the fluid and an evaporated aluminum coating on the far glass surface serves as an optically satisfactory mirror. The depth-averaged concentration field at any time can be deduced from the interference fringe pattern.

III. BUOYANCY DRIVEN CONVECTION

A. Local transport considerations

In thin-layer electrodeposition, the chemical reactions occurring at each electrode create gradients in ionic concentration [31]. When the cell is oriented in the usual horizontal configuration, the density gradients produced by these concentration gradients drive unavoidable fluid flow near each electrode. Since surfaces of constant density are not parallel to surfaces of constant pressure, buoyancy forces cannot be balanced in the absence of convection: a vanishing velocity field ($\mathbf{U} = \mathbf{0}$) is not a solution of the Navier-Stokes equations [32]. Metal ions depositing onto the cathode leave the solution nearby less concentrated and thus less dense. Low density fluid rises, driving an immediate and dramatic flow, as illustrated in Fig. 1(a). Convection is significant within a few seconds after initiation of an experiment; experiments typically last a few thousand seconds. A similar mechanism drives a sinking flow near the anode, where ions that are injected into the fluid raise the concentration and density. The two flows are independent, at least for short times and large electrode separation; in the absence of possible electric field effects, which will be discussed in Sec. IV, tracer particles far from either electrode display only Brownian motion. In Sec. III B we will consider the global nature of the convective motions, but first we consider the motion near the electrodes.

Figure 3(a) shows interferometric measurements of the density gradients responsible for buoyancy driven flow near the anode. The interferometer is adjusted to give a pattern of parallel, uniformly spaced linear interference fringes filling the field of view. The distorted interference pattern measured at some time during the experiment is compared to the uniformly spaced pattern recorded before current flows. The locations where interference fringes have been distorted by m original fringe spacings have experienced a density increase such that exactly m additional wavelengths now fit into the round-trip path length ($2w$) through the sample. By subtracting the undistorted fringe pattern at $t = 0$ from the distorted pattern at a later time, we can locate the curves of constant density [shown in Fig. 3(a)]. The concentration along one of these curves obeys

$$C = C_\infty + m\frac{\lambda_{\rm vac}}{2w(dn/dC)} = 0.2 + m(0.011)M, \quad (1)$$

where dn/dC is the rate of change of the refractive index with concentration ($dn/dC = 2.9 \times 10^{-2} M^{-1}$ for He-Ne light in $ZnSO_4$ [24]) and $\lambda_{\rm vac} = 632.8$ nm is the vacuum wavelength of He-Ne laser light.

The isoconcentration curves in Fig. 3(a) are not parallel to the electrode surface since diffusion is not the only transport process. Figure 3(b) shows the evolution of the concentration profile measured at mid-depth from Fig. 3(a); density gradients are quickly established by the chemical reaction occurring at the electrode surface. Interferometric techniques provide a noninvasive tool for studying the concentration field [24] and continue to shed light on the deposition process [33,55].

The strength of the buoyancy driven flow is illustrated by the velocity profiles in the horizontal and vertical directions shown in Fig. 4. For the 0.25-mm cell depth used in these measurements the maximum velocity near the electrode $v_{\rm max}$ is about 30 μm/s (for the conditions in Fig. 4). Hence the advective flux $Cv_{\rm max}$ is greater than the diffusive flux $D\nabla C$ for distances greater than $\sim$ 20 μm from the electrode surface. A characteristic time for the convective flow in the neighborhood of the electrode is $\tau \sim \pi d/4v_{\rm max} \sim 6$ s for the experiment of Fig. 4. Note in Figs. 4(c) and 4(d) that all circulation passes within $d/2$ of an electrode surface. The horizontal velocity component as a function of height has a slight

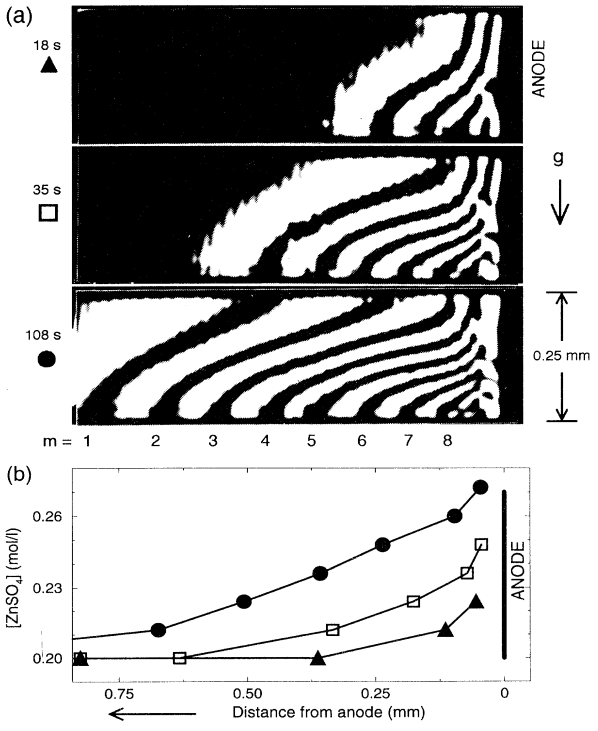

FIG. 3. (a) Interferometric measurement showing lines of constant density near the anode at three times. (b) The corresponding ionic concentration at mid-depth as a function of distance from electrode surface. (The cell is $18 \times 1 \times 0.25$ mm^3, [$ZnSO_4$]=0.2M, and $J = 40$ mA/cm^2.)

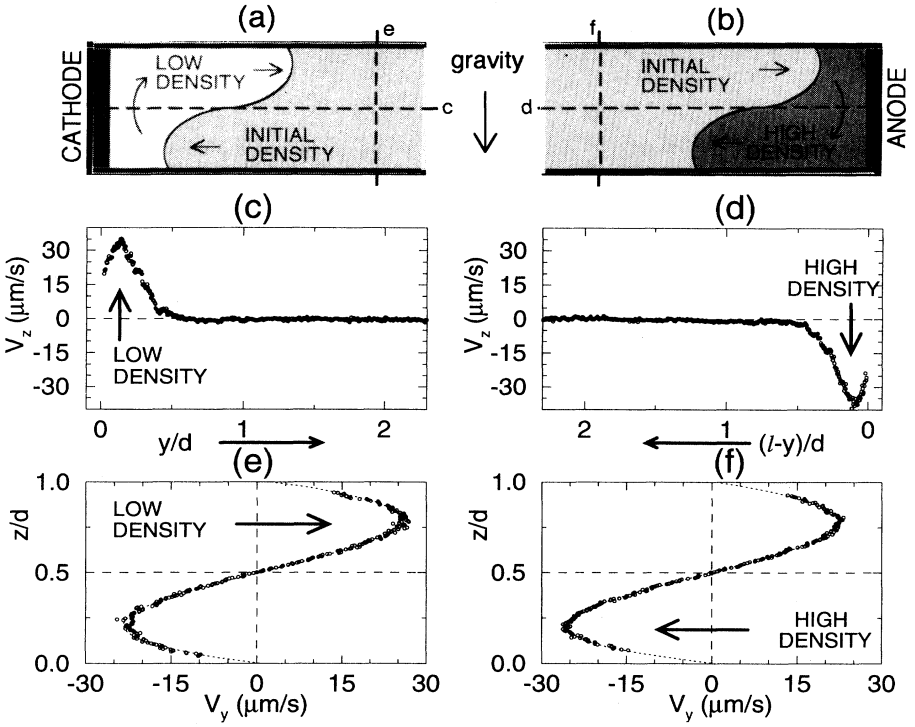

FIG. 4. (a) and (b) are schematic drawings indicating the density differences that drive the convective motion and the horizontal and vertical dashed lines indicate the location of the graphs of the velocity as a function of position shown in (c),(d), and (e),(f), respectively. ($t \approx 120$ s, the cell is $17 \times 1 \times 0.25$ mm^3, [$ZnSO_4$]=$0.2M$, and $J = 40$ mA/cm^2.)

asymmetry about the midplane; the flow away from either electrode comprises a faster, narrower plume than the return flow. This asymmetry is small in Fig. 4, but is quite pronounced at early times in a deeper cell, as Fig. 5 illustrates for a 1-mm-deep cell: the high density fluid leaving the anode spans only 40% of the cell depth and is 50% faster than the return flow of low density fluid; the maximum velocity is reached at about 15% of the cell depth.

At early times the flows near the anode and the cathode have the same structure. At longer times, however, when the solution near the cathode becomes depleted of ions, the growing, branching electrodeposit leads to a complicated flow at the cathode end of the cell while the flow remains simple near the anode. Hence our measurements of the convective velocity as a function of experimental parameters are made near the anode.

The time evolution of the fluid motion near the anode is shown in Fig. 6 for cells with four different gaps. The time scale of these measurements is long compared to the time for diffusion of momentum across the gap; even for the 1-mm-thick cell the viscous diffusion time $d^2/2\nu$ is

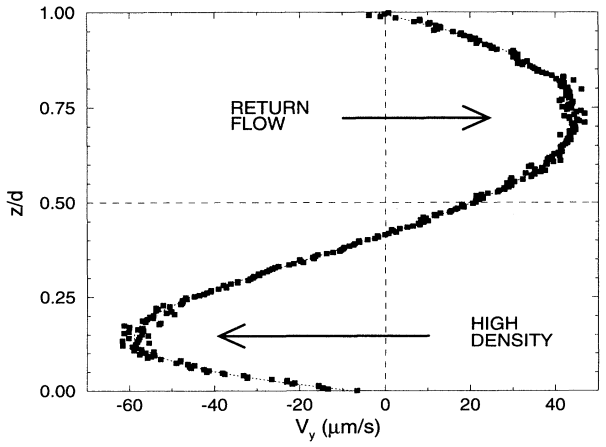

FIG. 5. Horizontal velocity component in a 1.0-mm-deep cell, showing the asymmetry as a function of depth. ($t \approx 90$ s, the cell is $17 \times 1 \times 1$ mm^3, $J = 40$ mA/cm^2, [$ZnSO_4$]=$0.2M$, and $y = 2$ mm from anode.)

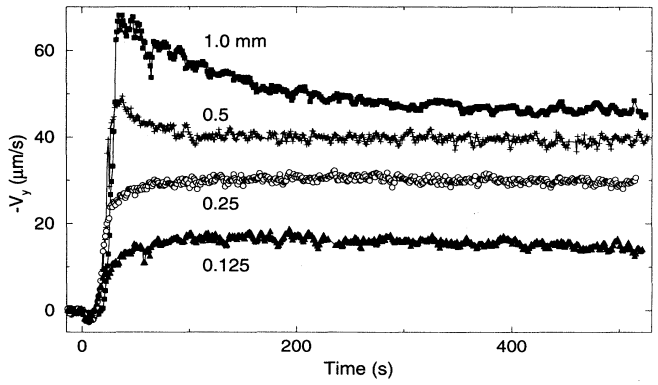

FIG. 6. Time evolution of the horizontal component of the velocity close to the anode for four different gap spacings, from the start of the experiment until the velocity reaches an asymptotic value. Measurements were made at a horizontal distance of $2d$ from the electrode, at the depth corresponding to the maximum in the velocity. (The cell is $100 \times 50 \times d$ mm^3, [$ZnSO_4$]=$0.1M$, and $J = 40$ mA/cm^2.)

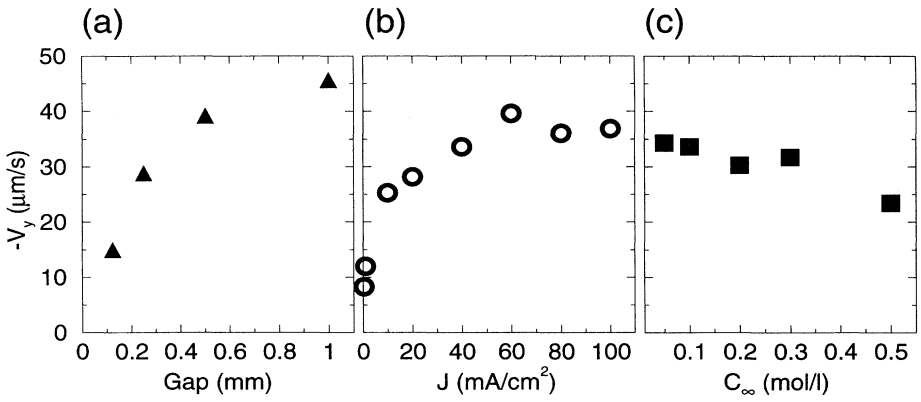

FIG. 7. Dependence of the buoyancy driven flow velocity at its maximum [see Fig. 4(f)] near the anode on experimental parameters: (a) plate separation (the cell is $100 \times 50 \times d$ mm^3, $J = 40$ mA/cm^2, $[ZnSO_4] = 0.1M$, and t=500 s), (b) current density ($[ZnSO_4] = 0.1M$, $d = 0.5$ mm, and $t = 900$ s), and (c) solution concentration ($J = 40$ mA/cm^2, $d = 0.5$ mm, and $t = 900$ s).

only $\sim$ 1 s; hence the convective disturbance fully fills the cell depth space as it propagates away from the electrode. (For comparison, the convective time scale τ is about 15 s for this 1-mm gap experiment.) The measurements in Fig. 6 were made at the depth corresponding to the maximum in the horizontal component of the velocity, at a horizontal distance of $2d$ from the anode. At this location tracer particle motion is reversed for approximately the first 20 s after the current is initiated and then velocity increases rapidly.

The reverse motion is due partly to electro-osmosis (see Sec. IV B), which is fluid flow driven by the instantaneously established electric field, and partly to a small electrophoretic drift of the tracer particles through the fluid. These electric field driven motions dominate during the first 20 s, while the density gradients responsible for buoyancy driven convection are still being established. After a few hundred seconds the velocity profile at a distance $2d$ from the anode is essentially time independent, as can be seen in Fig. 6. For small gaps the asymptotic velocity is approached from below, while for large gaps the velocity overshoots and approaches a final value from above.

The dependence of the asymptotic horizontal velocity maximum on plate separation d, average current density ($J = I/wd$), and bulk concentration C_∞ is shown in Fig. 7. As expected for buoyancy driven convection, the maximum velocity increases with increasing d and J and decreases slightly with increasing C_∞. The dynamic viscosity is concentration dependent, increasing about 24% as the molar concentration of our electrolyte solutions is raised from $0.05M$ to $0.5M$; this contributes to the decrease in flow speed as the bulk concentration is raised [34]. Note also that an asymmetry develops as an experiment proceeds: fluid viscosity is lowered by depletion close to the cathode but raised by the injection process near the anode.

B. Growth of the convection rolls

The region of density driven convection increases in time, invading the cell from both ends, as the sequence of plots of tracer particle trajectories in Fig. 8 illustrates. This sequence shows that the convection rolls develop independently near each electrode; during the time of this figure there is no significant convection in the central 70% of the cell, which is not shown. However, the convection rolls generated at the anode and cathode continue to grow and ultimately collide approximately 3000 s after the start of the experiment. This modifies significantly the global concentration distribution and the flow pattern. The collision of the oppositely growing convection rolls can lead to a change in the growth rate and in the morphology of the electrodeposit. Such changes have been previously linked to the arrival at the deposit of a *migratory* "front" of chemical impurities originating from the anode [15,17–20], but little consideration has been given to perturbations by *convective* fronts [21].

The full time evolution of the interacting modes of transport in electrodeposition is revealed by the striking space-time diagram in Fig. 9(a). This figure is constructed from digital gray scale images made with the camera viewing the electrodeposition cell from above. Measurements made each 10 s are averaged over 10% of the cell width (the x direction) to reduce each image to a line, and then these lines are stacked to yield the space-time image spanning the duration of the experiment (2500 s). Visualization of the different transport modes is accomplished by adding tracer particles, a small amount of sulfuric acid, and a color pH indicator to the electrolyte.

The "cathodic roll" is visible in Fig. 9(a) because the porous, growing cluster inhomogeneously filters incoming electrolyte, creating a nonuniform distribution of tracer particles in outflowing fluid. The zone of cathodic convection appears to grow sublinearly at first, but is quickly slaved to the linearly advancing electrodeposit.

The pH front is visualized using bromocresol green indicator. This indicator in zinc sulfate solution is colored yellow below pH 3.8 and changes to dark blue above pH 5.4. When sufficient sulfuric acid is added to $0.1M$ $ZnSO_4$ to move the electrolyte pH below 3.8, we found that we could visualize migratory transport directly. When an electric field $\mathbf{E}_\infty$ is impressed across the cell, protons are driven away from the anode with a

speed $\mathbf{v}_{H^+}$ proportional to their electrophoretic mobility μ_{H^+} ($\mathbf{v}_{H^+} = \mu_{H^+}\mathbf{E}_\infty$), leaving behind a zone of high pH. The pH front in Fig. 9(a) marks the boundary between the zone of ambient pH (light) and the higher pH zone depleted of migrating protons (dark). The nearly linear growth of the high pH zone indicates that the electric field changes little in the bulk electrolyte during galvanostatic growth. When the growing cluster encounters the high pH zone, the growth morphology changes, the branch tip color becomes visibly darker, and the growth speed decreases abruptly, as indicated by the change in slope of the cluster boundary near 700 s. This morphology transition, triggered by the arrival of a migratory front, is sometimes called the Hecker effect and has been examined in detail in recent years [15,17–21]. The space-time description used here visually captures the growth speed modification caused by the arrival of the pH front.

A second transition in the growth process occurs at about 1100 s, when the cluster encounters the moving, concentrated fluid in the anodic roll. The speed of growth decreases substantially, as can be seen in Fig. 9(a), though this second (convection-related) transition is more gradual than that triggered by the (migratory) pH front.

Our visualization of multiple transport modes makes it possible to distinguish transitions involving convection from those arising purely from migration. The very dark zone advancing behind the pH front defines the convecting anodic roll. We believe that the darker color results from a trapping of indicator molecules inside the roll. Looking through a microscope, we see streaming motion of the tracer particles confined to the darker colored portion of the high pH zone, with Brownian motion dominant in the lighter colored portion. The anodic roll initially grows according to a sublinear power law, as we shall show. At approximately 1000 s, the cathodic and

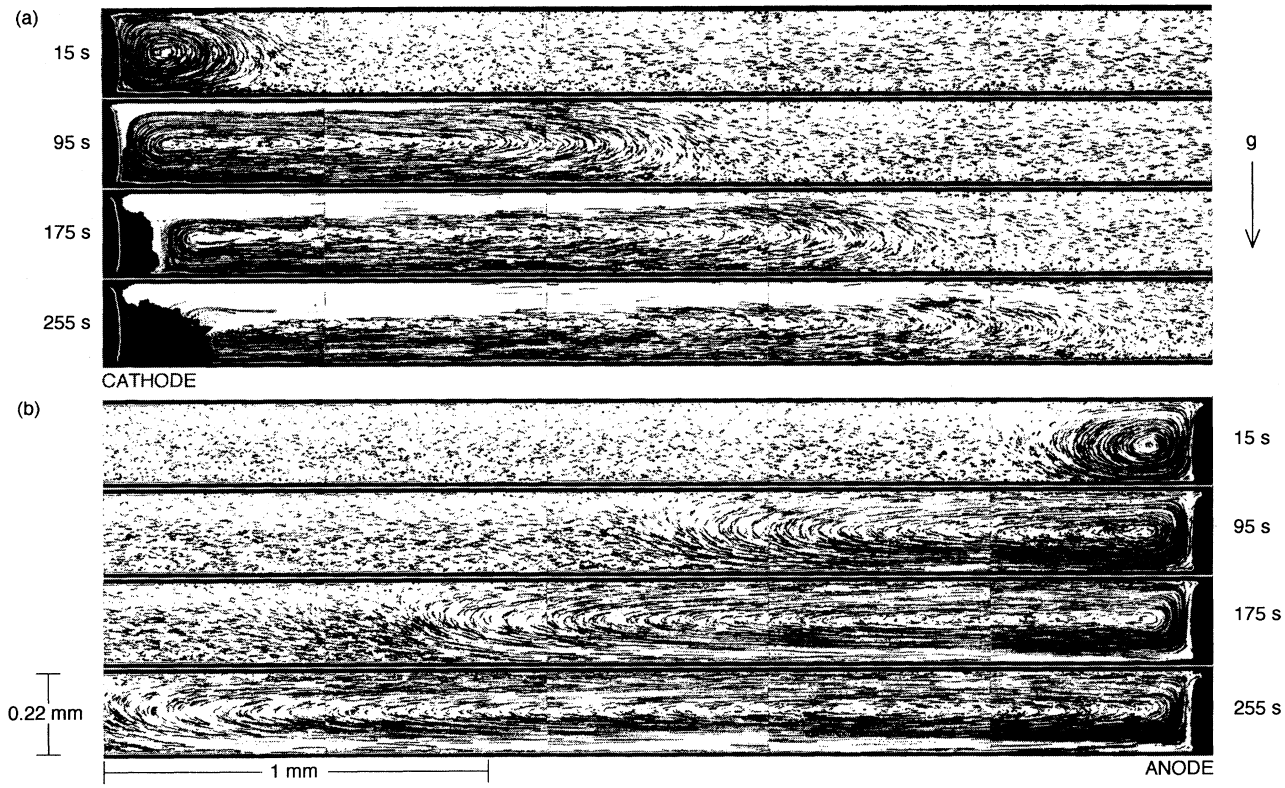

FIG. 8. Side view of electrodeposition showing the growth of convection rolls (a) near the cathode, where the depleted electrolyte rises and drives a clockwise flow, and (b) near the anode, where the electrolyte with high concentration falls and also drives a clockwise flow. The affinity of the growing cluster for the lower plate probably results from the combined effects of gravity acting upon the metallic electrodeposit and from preferential growth in the direction of the stronger concentration gradient that exists near the bottom of the cell in the presence of convection. In the cell center, away from the convection rolls, the tracer particles exhibit Brownian motion. These images are formed by superposing digital snapshots recorded over a 10-s interval, then aligning five images end to end to view the entire roll composite. The composites are labeled according to the time at which the end of the roll was in view. (The cell is $17 \times 1 \times 0.22$ mm^3, $[ZnSO_4]=0.2M$, and $J = 45$ mA/cm^2.)

anodic rolls collide and merge into a single convecting zone driven from both sides. Highly concentrated material previously trapped in the anodic roll is now entrained in the single roll and advects rapidly to the growth in the lower half depth of the cell. The nonuniform distribution of tracer particles that delimited the cathodic roll is similarly entrained after collision, advecting toward the anode in the upper half depth of the cell [see the curve labeled "after collision" in Fig. 9(a)].

Measurements of the concentration as a function of position in the cell, made by separating the cell into ten parts and titrating to determine the concentration of the zinc ions, are presented in Fig. 9(b). These measurements, made in a high purity cell without visualization additives, show that the concentration gradient is increased in the center of the cell after the collision of the anodic and cathodic rolls (cf. the measurements at 600 and 1260 s). The concentration profile abruptly changes curvature following roll merger, but thereafter evolves very little, and the cluster advances more slowly in the higher-concentration zone [see Fig. 9(a)].

The situation pictured in Fig. 9(a) is for a cell with large current density and large plate separation. In such cells, for smaller current density the material from the anodic roll can advect to the cluster *before* the migratory *p*H front is expected to arrive, perturbing the growth earlier than purely migratory considerations would suggest.

To characterize the advance of the anodic convective disturbance, we measure the roll size as the distance between the anode surface and the location beyond which tracer particles have no mean motion [35]. Measurements of the size of the anodic convection roll as a function of time for different cell depths reveal two distinct regimes, as Fig. 10 illustrates: the roll size grows as $t^{4/5}$

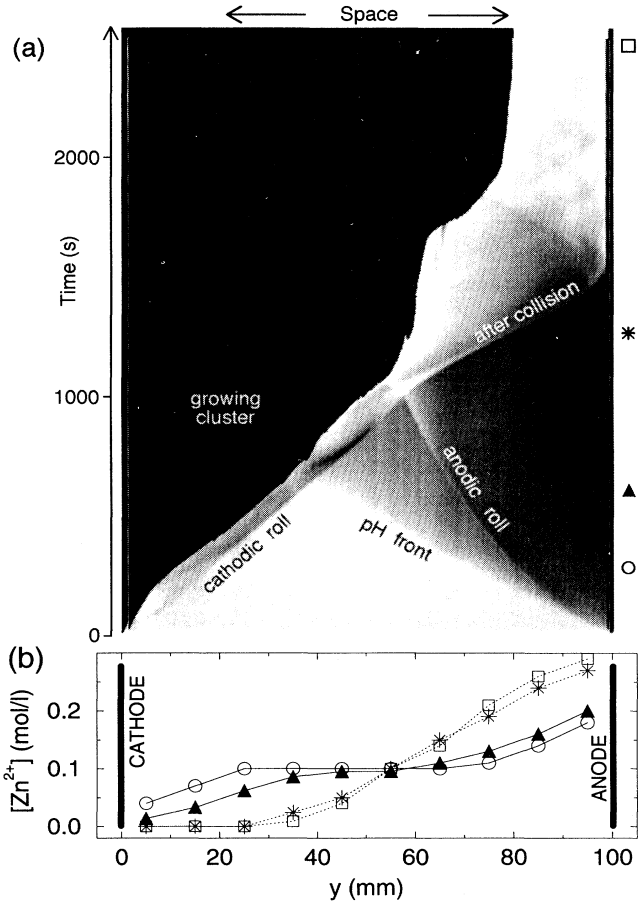

FIG. 9. (a) Space-time representation of a electrodeposition experiment showing the evolution of the metallic cluster, the migratory *p*H front, the cathodic convection roll, and the anodic convection roll. The change in growth rate of the cluster upon encountering the *p*H front is characteristic of the Hecker effect [17–20]. The growth speed also decreases sharply when the cluster encounters the highly concentrated anodic roll. (b) Concentration of zinc ions as a function of distance from the cathode, at four times: ○, 285 s; ▲, 600 s; ✱, 1260 s; and □, 2460 s, which are indicated with the respective symbols on the right-hand side of (a). (The cell is $100 \times 50 \times 1.0$ mm^3, [$ZnSO_4$]=0.1M, and $J = 100$ mA/cm^2.)

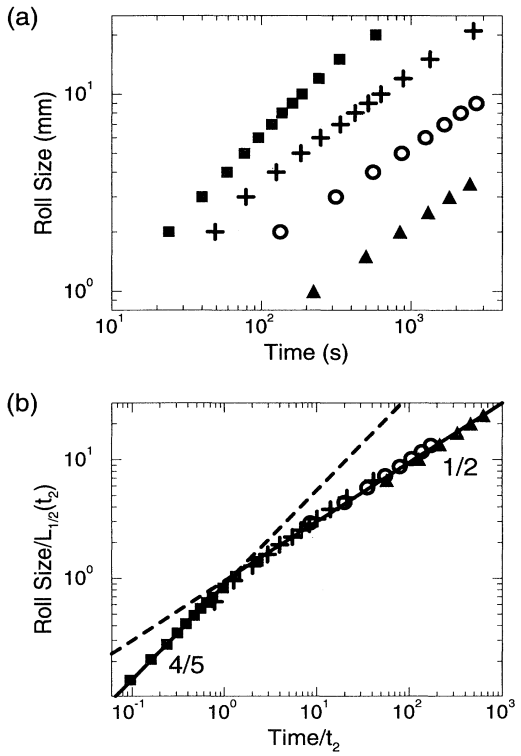

FIG. 10. Size of the convecting zone as a function of time for cells of different depths: (a) with dimensional size and time and (b) with time scaled by t_2, the molecular diffusion time across the fluid depth, and the roll size scaled by $L_{1/2}$ (cf. the text) evaluated at t_2. The roll size grows as $t^{4/5}$ at short times and as $t^{1/2}$ at long times. Cell depth: ■, 1.0 mm; +, 0.5 mm; ○, 0.25 mm; and ▲, 0.125 mm. (The cell is $100 \times 50 \times d$, [$ZnSO_4$]=0.1M, and $J = 40$ mA/cm^2.)

for short times and large gaps and as $t^{1/2}$ for long times and small gaps; the latter case is the most relevant to experiments in electrodeposition, which often seek to reduce convective effects by decreasing the plate separation. The observed dependence of the size of the convection roll on plate separation d [Fig. 11(a)], current density J [Fig. 11(b)], and time [Fig. 10(b)] (and the absence of a dependence on concentration [Fig. 11(c)]) can be combined into a single phenomenological relation that describes the behavior for the parameter range studied,

$$L_{1/2}(J,d,t) = \sigma J^{3/10} d^{6/5} t^{1/2}, \tag{2}$$

where the constant σ has the value 0.48 for L and d in cm, J in mA/cm^2, and t in seconds.

Some insight into the short-time behavior can be gained by considering the high-density fluid produced at the anode as a *gravity current* penetrating a lower-density fluid [36–38]. The $t^{4/5}$ evolution we see at early times in large gaps seems to follow from this approach, although the applicability of this formulation to electrodeposition [23] is clearly limited. We will describe the gravity current analysis of Huppert [36] and then examine the conditions under which the model could be applicable to convection in electrodeposition. Consider the penetration of a volume Q of dense fluid (e.g., oil; density ρ_0) into a rectangular chamber of lower density fluid (e.g., air; density ρ_∞). If the volume of high-density fluid present in the chamber is increased at a constant rate, then $Q = qt$, where q is the time-independent flux rate. This volume can be estimated by $Q \sim Lhw$, where w is the chamber width and L and h are estimates for the gravity current's length and height, respectively. Balancing the buoyancy force acting on the gravity current with the viscous drag on the current leads to the following scaling relations [39]:

$$L(t) \sim \left(\frac{g(\rho_0-\rho_\infty)q^3}{\rho_0 \nu w^3}\right)^{\frac{1}{5}} t^{\frac{4}{5}}, \tag{3}$$

$$h(t) \sim \left(\frac{q^2 \rho_0 \nu}{g(\rho_0-\rho_\infty)w^2}\right)^{\frac{1}{5}} t^{\frac{1}{5}}. \tag{4}$$

Can the invasion of the high-density fluid from the anode in electrodeposition be described by this formulation? Some important distinctions should be mentioned. In our case, the high-density zone is not of uniform density ρ_0, but rather the density is a function of space and time, determined by simultaneous solution of the time-dependent Navier-Stokes equations and the diffusion equation involving nonlinearly coupled convection and migration. Unlike the penetration of oil into air, here the high-density zone mixes readily with the low-density fluid. Under conditions of constant current deposition, a constant *mass flux* (not volume flux) is imposed at each electrode; only if the flow is fast can this be approximated as an introduction of a volume of uniform density. In a thin gap electrochemical cell h cannot grow without limit — the maximum value is d. Moreover, the electrochemical cell is closed so fluid cannot flow through the end walls and the return flow outside the gravity current is not negligible.

Despite these differences, if the convective flow were fast (compared to diffusion), high-density fluid created within $d/2$ of the anode surface could be advected away at such a high rate that the density throughout the gravity current would be nearly uniform (ρ_0; concentration C_0 throughout). This amounts to insisting that convection alone accounts for particle flux outside a thin diffusion layer at the electrode surface. In a deep cell this fast-moving high-density zone would be free to expand in depth during the early part of the experiment. Rosso *et al.* observed the $t^{4/5}$ growth of the cathodic convection zone in a 0.5-mm-deep cell during the early part of a constant current electrodeposition experiment [23]. The anodic flux rate analogous to that used in the cathodic study of Rosso *et al.* is $q = Jdw/zeN_A(C_0 - C_\infty)$, where ze is the Coulombic charge on a metal ion and $N_A = 6\times10^{23}$ ions/mole. The length of an anodic gravity current under galvanostatic conditions is then described by

$$L(t) \sim \left[\frac{g(\rho_0-\rho_\infty)}{\rho_0\nu}\left(\frac{Jd}{zeN_A(C_0-C_\infty)}\right)^3\right]^{\frac{1}{5}} t^{\frac{4}{5}}. \tag{5}$$

The $t^{4/5}$ scaling agrees with our observations for early times in experiments involving large gaps and fast flow. The dependences of the other parameters could not be confirmed since under the assumption of rapid advection, the concentration C_0 and the density ρ_0 established near the anode prior to the fluid motion increase with the current density, highlighting the complicated interplay

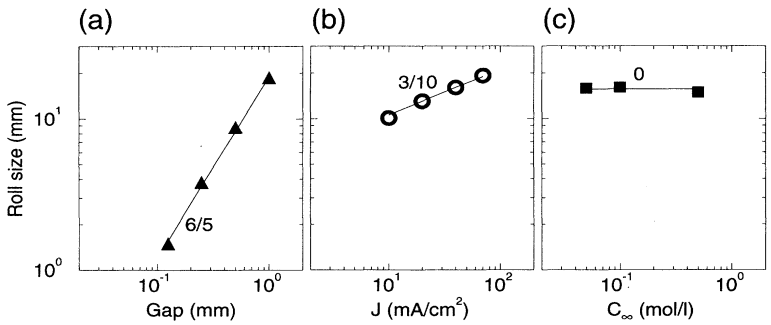

FIG. 11. Evolution of the anodic roll size during the $t^{1/2}$ regime as a function of (a) gap size (J = 40 mA/cm^2, [$ZnSO_4$]=0.1M, and t = 500 s), (b) current density ([$ZnSO_4$]=0.1M, d = 0.5 mm, and t = 1500 s), and (c) solution concentration (J = 40 mA/cm^2, d = 0.5 mm, and t = 1500 s). The slopes of the lines are given to indicate the power laws discussed in the text. (l = 100 mm, w = 50 mm.)

between diffusion and convection.

The assumptions leading to the $t^{4/5}$ scaling break down if diffusion establishes concentration variations over a large spatial region. With constant mass flux imposed at the electrode surface, the volume of the gravity current Q increases linearly in time only if its density remains constant in time, but the density ρ_0 at the anode surface *grows* in time when diffusion is important. Constant current experiments dominated by diffusion should have a $t^{1/2}$ growth of this surface density [31]. If the height h ceases to grow because of depthwise confinement and the density added increases like $t^{1/2}$, then both the volume Q and the length L of the high-density zone will grow as $t^{1/2}$.

Figure 10(b) shows that the data for the time dependence of the convection roll size in cells with different thicknesses d all collapse onto a single curve if the time and convection roll size are made dimensionless as follows: divide time by t_2, the time taken for molecular diffusion over a distance of $d/2$,

$$t_2 \equiv (d/2)^2/2D, \tag{6}$$

and divide the roll size by the phenomenological length $L_{1/2}$ evaluated at t_2. Figure 10(b) shows that data for different cell thicknesses make a transition from the 4/5 to the 1/2 scaling at the same point, which supports the choice of dimensionless variables. The $t^{4/5}$ scaling is seen only in thick cells at early times. In thin cells such as those used in most recent electrodeposition experiments, the convection roll size scales as $t^{1/2}$ from the beginning of an experiment. The relevance of the *vertical* molecular diffusion time t_2 to the rescaling of the roll advance emphasizes the three-dimensional character of electrodeposition growth experiments even in thin-gap cells.

IV. ELECTRIC FIELD DRIVEN CONVECTION

The action of the electric field on the ions in the electrolyte leads to migration and also convective effects. In electrochemistry these complications are often reduced by adding a high concentration of mobile ions, a *supporting electrolyte*, which increases the solution conductivity so that the effect of the electric field on species of primary interest can be neglected [31]. However, this technique has seen little success in thin-layer electrochemical deposition since supporting electrolytes perturb the branch structure over the long time scales typical to growth experiments. The chemistry is simpler without a supporting electrolyte, but the transport arising from the electric field is non-negligible. For example, when ionic migration is a significant transport mechanism, a transition in the morphology of the growth structure can occur [15,17–20]. For low electrolyte concentration the convective effects arising from a non-negligible electric field can be substantial in thin-layer electrochemical growth experiments.

A. Electroconvection

Bruinsma and Alexander [40] discussed the possibility of hydrodynamic flow generated solely by the action of the electric field on charges in an electrolytic cell, but they predicted flow velocities much smaller than those likely to arise preemptively from density gradients. It seemed doubtful that this electrohydrodynamic instability would be observable in experiment. However, Fleury *et al.* [25–28] developed a model in which charges surrounding a growing array of branches interact with the electric field to generate vortex pairs in the plane of the growth and they obtained images of the concentration field that qualitatively supported their picture. Now our velocity field measurements clearly reveal the vortex pairs, as Fig. 1(b) illustrates. In this section, we compare the prediction of Fleury *et al.* [27] with velocity measurements.

The vortex pairs are formed by the electrical force on space charge that accumulates near the branch tips, thus pulling ions towards the electrode and dragging fluid along [see Fig. 1(b)] [25–27]. The space charge near the branch tips contributed by the diffuse Gouy-Chapman portion ($\sim$ 10 nm thick) of the electric double layer [31] is supplemented by a larger zone of unbalanced positive charge ($\sim$ 1 μm thick) during steady-state electrodeposition, as Chazalviel has shown [14]. The porous metallic deposit allows fluid to penetrate the tips and be ejected from the sides, creating a counterrotating vortex pair at each branch tip. Electroconvective vortices rotate in the quasiplane of the growth, in contrast to buoyancy driven flow, which pierces this plane near the branches (rotation in a vertical plane). If the electric field is switched off, the electroconvection abruptly ceases (on the time scale of viscous diffusion), while buoyancy driven convection continues until concentration gradients are dissipated. Electroconvection is most easily observed in solutions of low ionic strength ($\sim 0.01M$), where the electric field is not strongly shielded and large concentration gradients cannot be established near the cathode (so that buoyancy driven flow is less significant).

In the model of Fleury *et al.* growing branches form a comblike array of infinitesimally thin, parallel conducting teeth, with space charge in the vicinity of each tip. Under assumptions of quasi-two-dimensionality and flow dominated by viscosity, the stream function in the reference frame moving with the tips involves a sum over the contributions of each tooth [26]

$$\psi(x,y) = V_a x + \frac{fd}{24\pi\rho\nu} \sum_{k=-\infty}^{+\infty} \frac{x - kb}{[(x-kb)^2 + y^2]}, \tag{7}$$

where V_a is the growth speed of the tips, taken to be equal to the anionic migration speed, f gives the strength of the force on the positive space charge in the fluid ($f > 0$) [41], d is the cell gap, b is the spacing between adjacent branches, k labels the branches in the infinite array, ρ is the fluid density, and ν is the kinematic viscosity. The unrealistic assumption of infinitesimal branch thickness leads to a singularity in the velocity at each branch tip. Fleury and co-workers [27] remove this singularity by separating the vortices generated on either side of a tip by a finite distance ($2a$) representative of the branch width. Defining r_{ka} as the distance to the vortex centered at $(kb + a, 0)$ and r_{-ka} as the distance to the vortex cen-

tered at $(kb-a,0)$,

$$r_{\pm ka}=\sqrt{(x-kb\mp a)^2+y^2}, \tag{8}$$

one obtains a stream function that [42] incorporates finite branch thickness into the model, recovering the infinitesimal-thickness expression in the limit $a\to 0$:

$$\psi(x,y)=V_a x+\frac{fd}{24\pi\rho\nu}\sum_{k=-\infty}^{+\infty}\frac{1}{2a}\ln\left(\frac{r_{-ka}}{r_{ka}}\right). \tag{9}$$

The two-dimensional velocity field $\mathbf{V}=(\partial\psi/\partial y, -\partial\psi/\partial x)$ is then given by

$$V_x=\frac{fd}{48\pi\rho\nu a}\sum_{k=-\infty}^{+\infty}\left(\frac{y}{{r_{-ka}}^2}-\frac{y}{{r_{ka}}^2}\right), \tag{10}$$

$$V_y=-V_a-\frac{fd}{48\pi\rho\nu a}\sum_{k=-\infty}^{+\infty}\left(\frac{x-kb+a}{{r_{-ka}}^2}-\frac{x-kb-a}{{r_{ka}}^2}\right). \tag{11}$$

The appropriate functional form for the force f has been the subject of some discussion in the literature [26,27], but the proposed forms have not been tested directly in experiments. Since the model velocity field described above seems to capture qualitative features of the flow, we fit the Fleury model to our data with f treated as a fitting parameter. Applying the particle tracking procedure outlined above to the sequence of images shown in Fig. 1(b) when viewed in the reference frame moving with the central tip [Fig. 12(a)], we obtain the velocity field throughout the field of view.

Our implementation of the model takes into account the three tips appearing in Fig. 12(a) and their six accompanying vortices (two are off screen to lower left and right). Each of the three branches makes a contribution to the velocity field of the following amount:

$$V_x=\frac{fd}{48\pi\rho\nu a}\left(\frac{y}{(x+a)^2+y^2}-\frac{y}{(x-a)^2+y^2}\right), \tag{12a}$$

$$V_y=-\frac{fd}{48\pi\rho\nu a}\left(\frac{x+a}{(x+a)^2+y^2}-\frac{x-a}{(x-a)^2+y^2}\right), \tag{12b}$$

where the calculation for each side branch is made in a frame translated to the current tip and rotated appropriately. The distance from a branch axis to the center of an experimental side vortex is taken to be the value of a for that branch. The parameter b does not enter explicitly in (12) since we perform a translation of coordinates when calculating the contribution for each branch. In the frame comoving with the central tip, the side branches (which grow at a relative angle) are not stationary and the calculation also takes into account this motion. The velocity of the moving frame of the central tip $V_a=10.7$ μm/s also contributes to the total calculated for V_y [as in (11)]. We include the small electrophoretic motion of the tracer particles (see Sec. IV B) by adding 2.3 μm/s to V_y. Figure 12(b) shows the flow simulated by the model when using the experimentally determined value of f.

We fit V_y measured along the path indicated by the vertical line in Fig. 12(b) to that predicted by the three-branch realization of the model, assuming the model values of f are equal for each branch. The model form fits the data well, as Fig. 13(a) demonstrates, yielding a best least-squares fit value for f: 4.7×10^{-10} N. Using this value of f, we can compare the velocity measured along a line parallel to the electrode with the prediction of the model, as shown in Figs. 13(b) and 13(c). The model provides a fair qualitative but poor quantitative description of these velocity measurements since the theoretical estimate for f proposed by others [26] is many orders of magnitude larger than the value we deduce experimentally.

The force parameter f can be estimated assuming steady-state deposition and zero fluid flow [26,27]

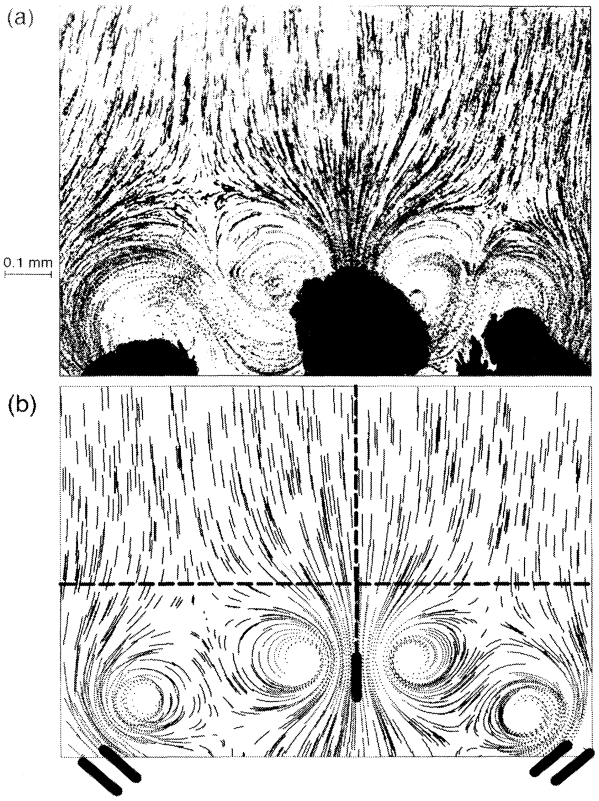

FIG. 12. (a) Experiment of Fig. 1(b) viewed in a reference frame moving with the central branch tip rather than in the laboratory frame. (b) Simulated particle streaks generated by the electroconvection model. Solid bars indicate the location and orientation of each branch tip at the beginning and end of a 6-s interval. (In this reference frame the side branches move slightly during the short time interval.) Velocity measurements along the dashed lines are compared in Fig. 13 to predictions of the model.

$$f_{\text{static}} = \left(1 + \frac{\mu_a}{\mu_c}\right) zeN_A C_\infty E_\infty b dx_1, \tag{13}$$

where μ_a and μ_c are the anionic and cationic mobilities, E_∞ is the magnitude of the electric field in the bulk ($\mathbf{V}_a = -\mu_a \mathbf{E}_\infty$), and x_1 is the thickness of the space charge layer. If the fluid is stationary, this thickness is estimated by [26]

$$x_1 = \left[\frac{9\epsilon\epsilon_0\mu_c(\delta U)^2}{8zeN_A C_\infty E_\infty(\mu_a + \mu_c)}\right]^{1/3}, \tag{14}$$

where $\epsilon = 78$ is the dielectric constant of the electrolyte and $\delta U \approx 1$ V is the voltage drop across the space charge layer. Using our experimental values ($C_\infty = 10^{-2}M$, $E_\infty = 130$ V/m, $b \sim 500$ μm, and $d = 100$ μm), we calculate $x_1 = 0.9$ μm and $f_{\text{static}} = 3 \times 10^{-5}$ N. The predicted velocities (~ 30 cm/s) are then 10^5 times larger than those observed in experiment.

The estimates given by Eqs. (13) and (14) are valid only for steady-state deposition without fluid flow however. Fleury *et al.* suggest that fluid flowing into the tip with speed V reduces the space charge layer thickness by a factor ξ [27],

$$\xi = \left[\frac{(\mu_a + \mu_c)E_\infty}{V + (\mu_a + \mu_c)E_\infty}\right]^{1/3}. \tag{15}$$

For our experiment, the inflow speed in the laboratory frame ($V = 38$ μm/s) reduces the force estimate by only 30%, so this correction alone cannot reconcile the factor of 10^5 disagreement with experiment.

Adding the contributions of even distant tips influences the flow pattern; thus the failure to consider every contributing branch leads to some error in our analysis. However, since the three branches we consider are well separated from other branches (the nearest branch is ~ 1300 μm from the central tip), this proves to be a small correction in our case. Including the contributions of two additional tips at ± 1300 μm, for example, increases the experimentally obtained value of f by only 4%. In this analysis, we do not include the contribution to fluid motion arising from electro-osmosis or the spatial variation of the tracer particle electrophoresis since both effects depend on the details of the electric field near the growing cluster (see Sec. IV B). We expect that the electro-osmotic contribution will be small near the growth in this 100-μm-deep cell, but the electrophoretic motion of the tracers through the fluid leads us to underestimate the fluid speed near the tips where the electric field is strong.

A more refined model incorporating the distribution of the charge near the cluster and the cluster shape would undoubtedly yield better correspondence with the observations. However, even a reduction of the space charge layer thickness to the 3-nm double-layer thickness appropriate for a $10^{-2}M$ electrolyte is still insufficient to account for the discrepancy, and it is difficult to believe that the charged layer is smaller than this. A more thorough understanding of the distribution of space charge near the tips seems necessary to obtain f.

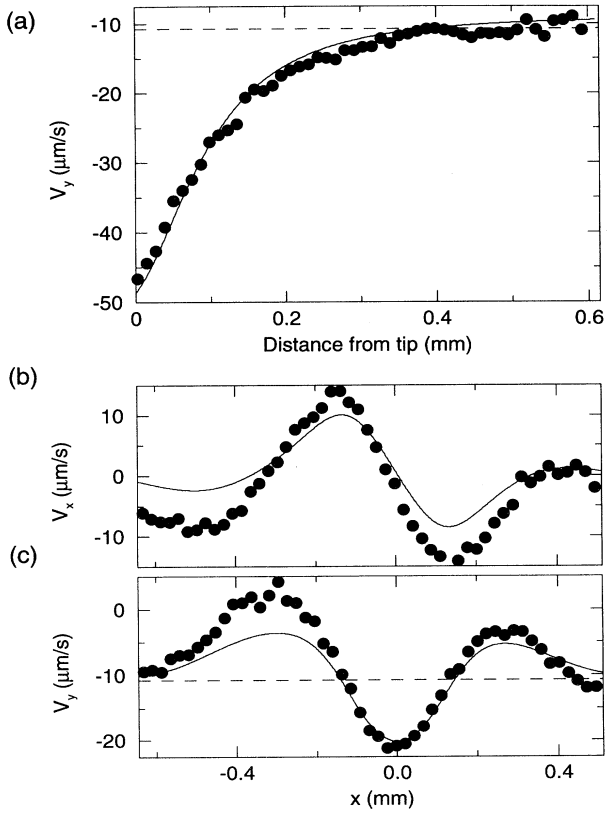

FIG. 13. Comparison of velocity measurements (●) with the electroconvection model (solid curves): (a) The model is fit to the data along the vertical line indicated in Fig. 12(b). (b) and (c) The value of f obtained in (a) is used to compare the model with measurements of two components of velocity measured along the horizontal line indicated in Fig. 12(b), 0.15 mm ahead of the center tip.

B. Electro-osmosis

Electro-osmosis [43–48] is another convective effect associated with the electric field in thin-layer electrodeposition experiments. This fluid motion arises when unbalanced charge residing in the solution near the confining surfaces of the electrodeposition cell moves in response to the electric field. This charge constitutes the diffuse part of the electric double layer at the electrolyte-boundary interface. The amount and the sign of this charge depend on the material used for the cell boundaries, how that material is treated before the cell is assembled (for example, rubbing or etching the surface), and on the properties of the solution (including pH). For an aqueous solution at a clean glass surface, the charge in the liquid very near the plate will be positive (H_3O^+) [44,45]. The applied electric field acting parallel to the fluid-glass interface during electrodeposition tends to move this charge to-

ward the cathode, dragging fluid along, creating a flow at the surface of each plate. If the cell is closed, the incompressibility condition leads to the generation of a pressure gradient across the length of the cell, driving a return flow toward the anode at the center depth of the cell. The velocity profile is parabolic as a function of z with nonzero speed at each boundary [48,49], contrary to the usual no-slip boundary condition; the return flow at the cell center is of course in the opposite direction. It is important to emphasize that the fluid itself moves at the glass (at a distance corresponding to the double-layer thickness, a few molecular diameters), leading to an unusual *slip* boundary condition there [46].

The parabolic velocity profile of Fig. 14 shows the presence of electro-osmotic fluid motion in thin-layer electrodeposition. The observed motion of tracer particles results from the combination of electro-osmotic flow of the fluid (parabolic in z) and electrophoretic drift of the tracer particles through the fluid (uniform in z). The profile shows fluid motion toward the cathode near both confining glass plates and return flow toward the anode near mid-depth. The measurement is made at $x = w/2$ and far from either electrode at $y = l/2$; gravity currents will not arrive here for some time and, since no branch tips are nearby, electroconvection as discussed above cannot account for the motion here. The flow of Fig. 14 starts abruptly upon initiation of the electric current (prior to the emergence of branch tips from the distant cathode). The flow reverses immediately ($d^2/2\nu = 0.08$ s) if the current is reversed and stops immediately when the current is discontinued. We observe qualitatively similar behavior using other tracer particles (latex beads and oil drops) and using tracer particle seeding densities varying over three orders of magnitude. The parabolic shape

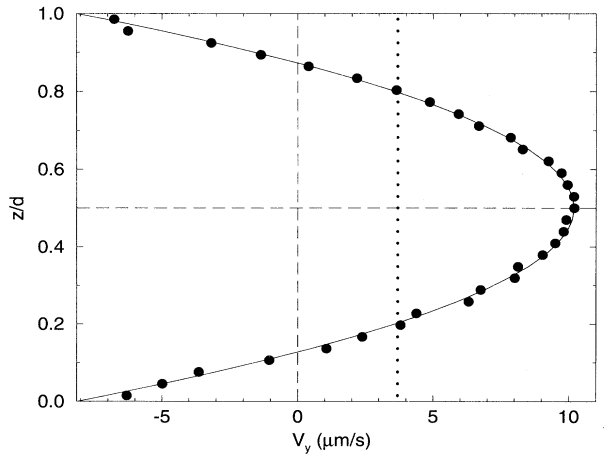

FIG. 14. Parabolic shape of the horizontal velocity as a function of depth measured far from either electrode indicates electro-osmotic fluid motion. The measured particle speed is the superposition of electrophoretic drift of the tracer particles *through* the fluid (3.7 μm/s toward anode, indicated by dotted line) and the flow of the fluid itself. (The cell is $34 \times 8 \times 0.4$ mm^3, [$CuSO_4$]=0.01M, and $J = 6.4$ mA/cm^2.)

of the profile, the slip condition observed near the wall with opposite flow near the mid-depth, and the behavior when varying the current level confirm the presence of electro-osmotic fluid motion.

An accurate estimation of the electro-osmotic fluid velocity at the wall u_{eo} and the electrophoretic motion of the particles u_{eph} requires accounting for the finite width of the confining cell using the correction of Komagata [47,50]. When expressed in our coordinates, the velocity profile measured at $x = w/2$, valid if $w/d > 15$ is

$$V_y = u_{eo}\left[1 - \frac{6}{1 - \frac{192d}{\pi^5 w}}\left(\frac{z}{d}\right)\left(1 - \frac{z}{d}\right)\right] + u_{eph}. \quad (16)$$

Fitting our data to this expression, we find $u_{eo} = -11.8$ μm/s and $u_{eph} = 3.7$ μm/s under these conditions of electric field and solution concentration.

Electro-osmosis may have also contributed to effects seen far from the growth by Fleury *et al.*, who "noticed that there is a global and quite slow motion of the tracers towards the anode [26]," though without observation of reverse flow near the plates, the motion as described cannot be distinguished from particle electrophoresis.

Immediately after initiation of the electric field, the most vigorous electro-osmotic flow occurs midway between the two electrodes ($y = l/2$) because the electro-osmotic flow in the y direction must go to zero at the impervious wire electrodes. The electro-osmotic flow should primarily occur ahead of the growth, where the electric field parallel to the glass is substantial. Behind the growing interface, in the region containing the metallic cluster, the osmotic effect is small because the electric field is small there. Even far from the electrodes, where the electro-osmotic effect is greatest, the flow velocities induced by electro-osmosis are small. Near the electrodes the electro-osmotic flow is often negligible compared to buoyancy driven convection or electroconvection.

The motion of particles toward the anode seen in the early moments of the measurements of Fig. 6 is a combination of electrophoretic particle drift and electro-osmotic fluid motion. Although the same field is applied for all four experiments, the mean particle motion during reversal depends on the gap, with fastest flow for $d = 0.25$ mm. Like electroconvection, electro-osmotic flow decreases as bulk concentration is increased; hence for the higher concentration of Fig. 6 this flow is weak and is quickly dominated by buoyancy effects. Attempts to compare electrodeposition experiments to the diffusion limited model are typically made in the low-concentration limit, but in this limit the fluid motion induced by electro-osmosis is most significant.

Our observation of electro-osmotic convection in growth experiments adds another convective effect to the list of nondiffusive processes in electrodeposition. Near an electrode this flow is often small compared to buoyancy driven convection and electroconvection, but it can significantly modify the global transport and certainly adds further complexity to the analytical treatment of electrochemical growth experiments.

V. DISCUSSION

We have shown that buoyancy effects inevitably drive fluid motion near each electrode in electrodeposition and have presented measurements indicating the way experimental parameters influence the flow speed and the extent of these convecting zones. Our thin-gap electrodeposition cell permits a clear side view of this flow and interferometric measurements show the resulting structure of the concentration field [55]. We have presented an empirical expression (2) for the location of the advancing edge of the anodic convection zone. In our examination of electroconvection we find qualitative agreement (but quantitative discrepancy) with the predictions of the model proposed by Fleury *et al.* We have also shown that an additional electric field related convection mode, electroosmosis, can be non-negligible in electrochemical growth experiments.

Convection certainly adds to the complexity of the electrodeposition problem. Hence it is reasonable to attempt to reduce convection to a negligible level. One possibility for controlling buoyancy driven flows is to orient the cell vertically with the cathode (and low-density fluid) above the anode (and high-density fluid). With this technique, the invasion of the cell by advancing gravity currents can be avoided, but convection produced by the electric field will remain. In this vertical orientation, the fluid is stabilized by the density stratification and gravity drives no fluid motion as long as there is no growth. The situation changes as soon as growth occurs because the concentration of fluid near a downward growing tip is lowered, thus establishing a horizontal concentration gradient that drives convection. During the ensuing growth competition, this convective motion feeds branches that are losing until those branches catch up with the leader. Hence, as Fig. 15(a) illustrates, with this orientation of the cell the convection inhibits competition between branches, leading to a uniform front of the growing tips rather than a hierarchy of branch sizes as seen in a horizontal cell [Fig. 15(b)]. A vertical cell with the anode (and high density fluid) above the cathode is unstably stratified and global convective circulation leads to a growth strongly affected by nondiffusive processes, as Fig. 15(c) illustrates. The addition of a *p*H indicator aids visualization of light, low-density plumes that rise from the cathode and dark, concentrated plumes that descend from the anode; see Fig. 15(d). In summary, convection arises for all cell orientations; no orientation yields growth governed solely by diffusion. A hierarchical electrodeposit structure forms only for a horizontal orientation.

Reducing the plate separation is the most common scheme for minimizing the effects of convection, but fluid concentration gradients *always* lead to a buoyancy driven flow during electrochemical growth in a gravitational field. The effect of fluid motion can be reduced by using a small plate separation, but separations below 50 μm can alter the morphology of the growth pattern [51]. There can be substantial convection even in cells only $50-100$ μm deep. Reducing the electrolyte concentration increases the importance of electric field driven convection relative to buoyancy driven flow, although decreasing the applied current density drives a weaker flow in both cases.

Another approach to suppressing convection is to use a gel medium impregnated with a metal salt [23,52], but

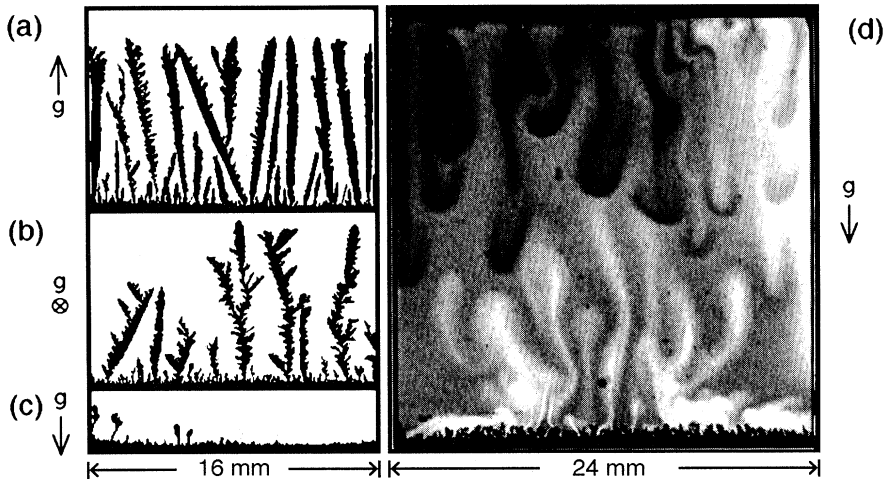

FIG. 15. Electrodeposition in cells of different orientations with respect to gravity: (a) vertical cell with the cathode (and low density fluid) at the top of the cell and the anode at the bottom; (b) a horizontal cell, which is the usual orientation of cells in electrodeposition experiments; and (c) vertical cell with the cathode (and low density fluid) at the bottom of the cell. (d) Plumes in (c), visualized with a *p*H indicator. The solutions used for (a)–(c) were deoxygenated by bubbled nitrogen. (The cell is $25 \times 25 \times 0.25$ mm^3, [$ZnSO_4$]=0.1M, and $J = 40$ mA/cm^2.)

this introduces other problems. Wang *et al.* [52] observed a significant morphology change for copper deposition from an agarose gel rather than from a liquid. Even in a liquid, small quantities of impurities can dramatically change the growth structure and in a gel the growth is also perturbed mechanically by the web of polymer linkages. Thus, while a gel can be used to suppress convection, it introduces other effects that must be considered. Similarly, Hibbert and Melrose used filter paper support to reduce convective effects, but they noted that the filter paper fibers affected the progress of growth [53].

In the gravity-free environment of space, electrodeposition experiments would be undisturbed by buoyancy driven flow, but would still be perturbed by fluid motion induced by the electric field if the electrolyte concentration is low. The use of a high electrolyte concentration in a microgravity environment, however, could effectively minimize both classes of convection and experiments involving larger plate separations would be possible with negligible convection.

There is recent evidence indicating that *electroless deposition* offers a promising scheme for studying electrochemical growth patterns with minimal convective perturbations [10,54]. The spontaneous deposition from a silver nitrate solution onto a copper electrode has been found to yield a growth regime and a pattern structure closely approximated by a purely diffusive description when the plate separation was kept small (50 μm). In this case, density gradients are much smaller (but still present) and there is no globally applied electric field. Convection is not entirely eliminated even in this case, but it seems to be so weak that diffusive transport dominates. Wavelet transform analysis [10] reveals structural features common to both electroless deposits and diffusion limited aggregation patterns (e.g., fivefold symmetry and a statistical hierarchical Fibonacci ordering).

In conclusion, any study of electrodeposition *must* consider the convective effects that inevitably arise because of gravitational and electric fields. In some cases proper consideration of convective transport can lead to insights into electrodeposition growth processes.

ACKNOWLEDGMENTS

We thank F. Leal of Centre de Recherche Paul Pascal for kindly providing the tracer particles; M. S. Pervez, T. H. Solomon, and P. B. Umbanhowar of the University of Texas for technical assistance with the particle tracking procedures used for velocity field measurements; and A. Arneodo, M. Marder, M. E. L. Oakes, and R. Bonnecaze for fruitful discussions. The work of J.M.H. and H.L.S. was supported by the U.S. Department of Energy Office of Basic Energy Sciences Grant No. DE-FG03-93ER14312 and by the Robert A. Welch Foundation Grant No. F-805. The work of A.K. and F.A. was supported by DRET Contract No. 93/0409 and CNES Contract No. 92/097. The work of A.K. was also supported by the Pinguin Foundation. The Texas-Bordeaux collaboration was supported by NATO Grant No. RG 900685.

[1] T. Vicsek, *Fractal Growth Phenomena* (World Scientific, Singapore, 1992) and references therein.
[2] *Growth Patterns in Physical Sciences and Biology*, edited by J. M. Garcia-Ruiz, E. Louis, P. Meakin, and L. M. Sander (Plenum, New York, 1993) and references therein.
[3] T. A. Witten and L. M. Sander, Phys. Rev. Lett. **47**, 1400 (1981).
[4] R. M. Brady and R. C. Ball, Nature (London) **309**, 225 (1984).
[5] M. Matsushita, M. Sano, Y. Hayakawa, H. Honjo, and Y. Sawada, Phys. Rev. Lett. **53**, 286 (1984).
[6] F. Argoul, A. Arneodo, G. Grasseau, and H. L. Swinney, Phys. Rev. Lett. **61**, 2558 (1988).
[7] A. Arneodo, Y. Couder, G. Grasseau, V. Hakim, and M. Rabaud, Phys. Rev. Lett. **63**, 984 (1989); A. Arneodo, F. Argoul, Y. Couder, and M. Rabaud, in *Growth and Form, Nonlinear Aspects*, edited by M. Ben Amar, P. Pelce, and P. Tabeling (Plenum, New York, 1991), p. 297.
[8] A. Arneodo, F. Argoul, J. F. Muzy, and M. Tabard, Phys. Lett. A **171**, 31 (1992).
[9] A. Arneodo, F. Argoul, E. Bacry, J. F. Muzy, and M. Tabard, Phys. Rev. Lett. **68**, 3456 (1992).
[10] A. Kuhn, F. Argoul, J. F. Muzy, and A. Arneodo, Phys. Rev. Lett. **73**, 2998 (1994).
[11] R. M. Suter and P. Wong, Phys. Rev. B **40**, 4536 (1989).
[12] F. Argoul, J. Huth, P. Merzeau, A. Arneodo, and H. L. Swinney, Physica D **62**, 170 (1993).
[13] D. G. Grier and D. Mueth, Phys. Rev. E **48**, 3841 (1993).
[14] J.-N. Chazalviel, Phys. Rev. A **42**, 7355 (1990).
[15] N. Hecker, D. G. Grier, and L. M. Sander, in *Fractal Aspects of Materials*, edited by R. B. Laibowitz, B. B. Mandelbrot, and D. E. Passoja (Materials Research Society, University Park, PA, 1985).
[16] P. P. Trigueros, J. Claret, F. Mas, and F. Sagués, J. Electroanal. Chem. **312**, 219 (1991).
[17] P. Garik, D. Barkey, E. Ben-Jacob, E. Bochner, N. Broxholm, B. Miller, B. Orr, and R. Zamir, Phys. Rev. Lett. **62**, 2703 (1989).
[18] J. R. Melrose, D. B. Hibbert, and R. C. Ball, Phys. Rev. Lett. **65**, 3009 (1990).
[19] V. Fleury, M. Rosso, and J.-N. Chazalviel, Phys. Rev. A **43**, 6908 (1991).
[20] A. Kuhn and F. Argoul, J. Electroanal. Chem. **371**, 93 (1994).
[21] A. Kuhn and F. Argoul, Phys. Rev. E **49**, 4298 (1994).
[22] F. Argoul and A. Kuhn, J. Electroanal. Chem. **359**, 81 (1993).
[23] M. Rosso, J.-N. Chazalviel, V. Fleury, and E. Chassaing, Electrochim. Acta **39**, 507 (1994).
[24] D. P. Barkey, D. Watt, Z. Liu, and S. Raber, J. Electrochem. Soc. **141**, 1206 (1994).
[25] V. Fleury, J.-N. Chazalviel, and M. Rosso, Phys. Rev. Lett. **68**, 2492 (1992).
[26] V. Fleury, J.-N. Chazalviel, and M. Rosso, Phys. Rev. E **48**, 1279 (1993).

[27] V. Fleury, J. Kaufman, and B. Hibbert, Phys. Rev. E **48**, 3831 (1993).
[28] V. Fleury, J. H. Kaufman, and D. B. Hibbert, Nature (London) **367**, 435 (1994).
[29] The latest version of NIH-IMAGE for Macintosh is available through Internet via anonymous ftp in directory /pub/image of zippy.nimh.nih.gov.
[30] M. S. Pervez and T. H. Solomon, Exp. Fluids **17**, 135 (1994).
[31] A. J. Bard and L. R. Faulkner, *Electrochemical Methods, Fundamentals and Applications* (Wiley, New York, 1980).
[32] D. J. Tritton, *Physical Fluid Dynamics* (Van Nostrand Reinhold, New York, 1977).
[33] F. Argoul, E. Freysz, A. Kuhn, C. Léger, and L. Potin (unpublished).
[34] In the present experiments the variations in viscosity are due primarily to concentration variations. The effect of temperature variations and the tracer particles is small. (The volume fraction of the tracer particles is $\sim 0.04\%$.)
[35] Far from either electrode the particles still move slightly due to electro-osmosis and electrophoresis (see Sec. IV B), but these motions are small and easily distinguishable from the buoyancy-driven flow of the advancing roll.
[36] H. E. Huppert, J. Fluid Mech. **121**, 43 (1982).
[37] N. Didden and T. Maxworthy, J. Fluid Mech. **121**, 27 (1982).
[38] J. E. Simpson, *Gravity Currents: In the Environment and the Laboratory* (Ellis Horwood, Chichester, 1987).
[39] As we are interested in the power-law behavior, we omit factors of order unity, as well as references to the shape function describing the gravity current's height; see Ref. [36] for a more detailed analysis.
[40] R. Bruinsma and S. Alexander, J. Chem. Phys. **92**, 3074 (1990).
[41] Our sign conventions follow that of Ref. [27] so that $\mathbf{f} = -f\mathbf{j}$ and $\mathbf{E}_\infty = -E_\infty \mathbf{j}$. This convention differs from that used in [14], requiring the right-hand side of Eq. (14) to have a positively signed denominator.
[42] The contribution to the stream function of each finite-thickness branch must take the form $(1/2a)\ln(r_{-ka}/r_{ka})$ to recover the infinitesimal-thickness stream function in the limit $a \to 0$. There is a factor of -2 error in [27], which gives this contribution as $(-1/4a)\ln(r_{-ka}/r_{ka})$.
[43] J. Th. G. Overbeek, in *Colloid Science*, edited by H. R. Kruyt (Elsevier, Amsterdam, 1952).
[44] *Electrophoresis, a Survey of Techniques and Applications, part A*, edited by Z. Deyl (Elsevier, Amsterdam, 1979).
[45] P. Jandik and G. Bonn, *Capillary Electrophoresis of Small Molecules and Ions* (VCH, New York, 1993).
[46] S. S. Dukhin and B. V. Deryaguin, in *Surface and Colloid Science, Volume 7*, edited by E. Matijevic (Wiley, New York, 1974).
[47] R. J. Hunter, *Zeta Potential in Colloid Science* (Academic, London, 1981).
[48] R. J. Hunter, *Foundations of Colloid Science* (Clarendon, Oxford, 1989), Vol. 2, p. 788.
[49] The fixed layer (inner Helmholtz layer) right at the glass surface does not move, so, strictly speaking, there is no slip at the boundary. However, the charges residing 1–10 nm from the glass surface (in the diffuse outer layer) are forced to move at the electro-osmotic velocity. Since this distance is small compared to typical cell dimensions, the fluid appears to move with the electroosmotic velocity right up to the wall. A Poiseuille flow treatment is therefore appropriate, with constant velocity boundary conditions applied 1–10 nm inside all physical confining walls.
[50] J. D. Hamilton and T. J. Stevens, J. Colloid Interface Sci. **25**, 519 (1967).
[51] W. Y. Tam and J. J. Chae, Phys. Rev. A **43**, 4528 (1991).
[52] M. Wang, N. Ming, and P. Bennema, Phys. Rev. E **48**, 3825 (1993).
[53] D. B. Hibbert and J. R. Melrose, Phys. Rev. A **38**, 1036 (1988).
[54] Alexander Kuhn, Ph.D. dissertation, University of Bordeaux, 1995.
[55] John M. Huth, Ph.D. dissertation, University of Texas at Austin, 1995.

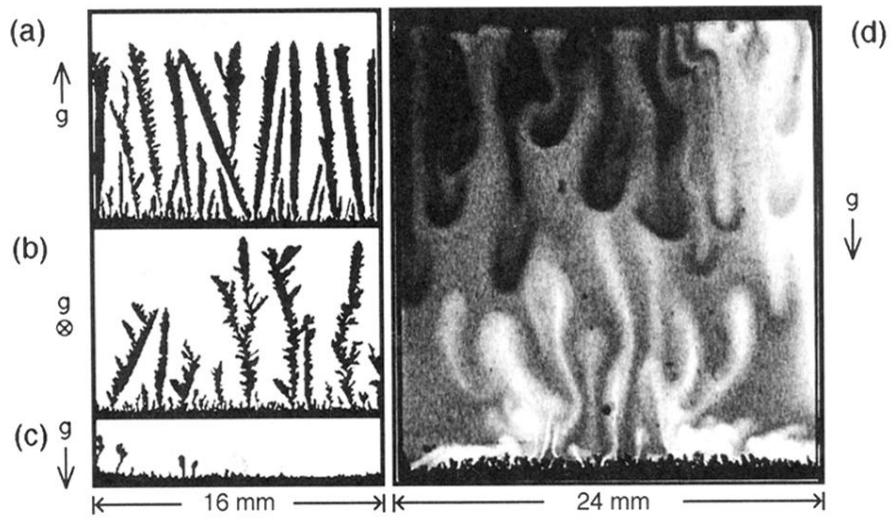

FIG. 15. Electrodeposition in cells of different orientations with respect to gravity: (a) vertical cell with the cathode (and low density fluid) at the top of the cell and the anode at the bottom; (b) a horizontal cell, which is the usual orientation of cells in electrodeposition experiments; and (c) vertical cell with the cathode (and low density fluid) at the bottom of the cell. (d) Plumes in (c), visualized with a *p*H indicator. The solutions used for (a)–(c) were deoxygenated by bubbled nitrogen. (The cell is $25 \times 25 \times 0.25$ mm^3, [$ZnSO_4$]=$0.1M$, and $J = 40$ mA/cm^2.)

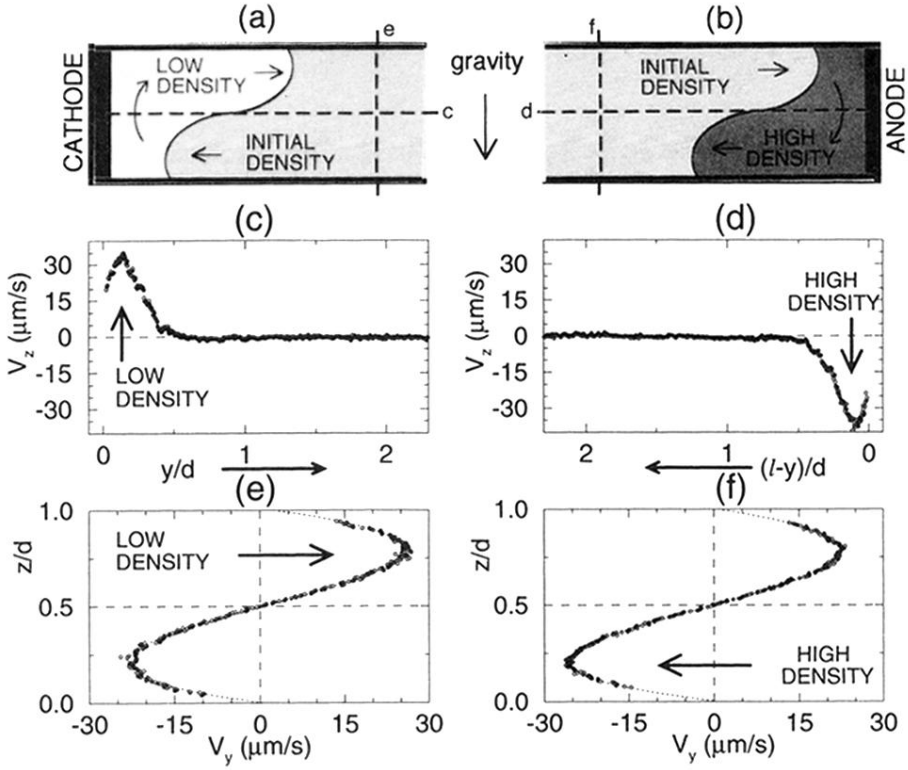

FIG. 4. (a) and (b) are schematic drawings indicating the density differences that drive the convective motion and the horizontal and vertical dashed lines indicate the location of the graphs of the velocity as a function of position shown in (c),(d), and (e),(f), respectively. ($t \approx 120$ s, the cell is $17 \times 1 \times 0.25$ mm^3, $[ZnSO_4]$=0.2M, and $J = 40$ mA/cm^2.)

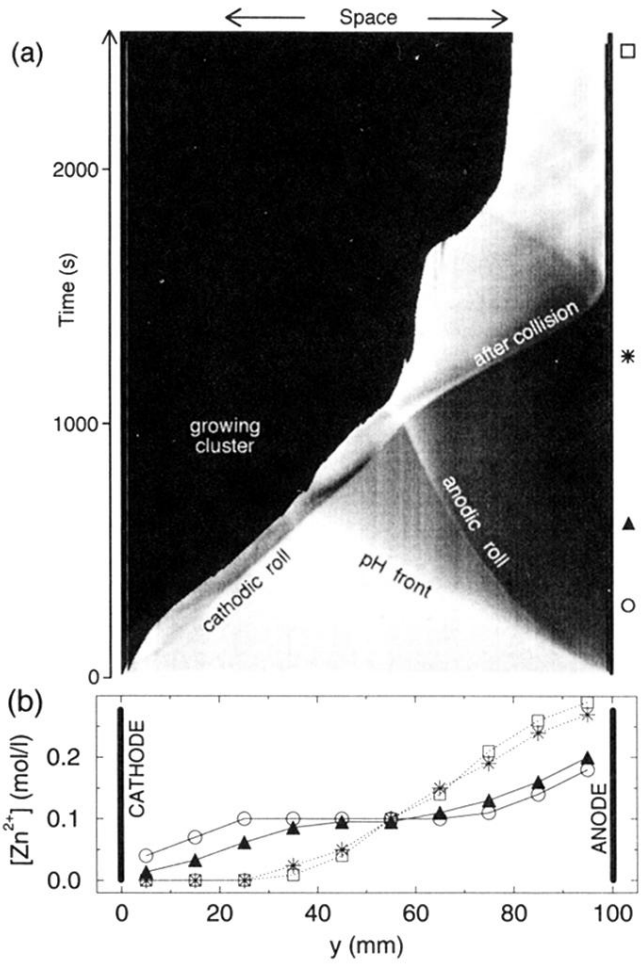

FIG. 9. (a) Space-time representation of a electrodeposition experiment showing the evolution of the metallic cluster, the migratory pH front, the cathodic convection roll, and the anodic convection roll. The change in growth rate of the cluster upon encountering the pH front is characteristic of the Hecker effect [17–20]. The growth speed also decreases sharply when the cluster encounters the highly concentrated anodic roll. (b) Concentration of zinc ions as a function of distance from the cathode, at four times: ○, 285 s; ▲, 600 s; ✱, 1260 s; and □, 2460 s, which are indicated with the respective symbols on the right-hand side of (a). (The cell is $100 \times 50 \times 1.0$ mm^3, [$ZnSO_4$]=0.1M, and $J = 100$ mA/cm^2.)